



Design and analysis of extruded quadrupolar dielectrophoretic traps

J. Voldman^{a,*}, M. Toner^b, M.L. Gray^a, M.A. Schmidt^a

^a *Department of Genetics, Massachusetts Institute of Technology, Boston, MA 02115, USA*

^b *Center for Engineering in Medicine, Massachusetts General Hospital, Boston, MA 02114, USA*

Received 18 March 2002; received in revised form 28 June 2002; accepted 2 July 2002

Abstract

We present the design and experimental analysis of a dielectrophoretic trap composed of four microfabricated gold posts excited in a quadrupolar fashion. Using quantitative modeling tools, we have designed these extruded traps to attain strong holding against flow while being constrained by a set of system parameters. The extruded geometry consists of cylindrical electrodes in a trapezoidal arrangement and substrate-interconnect shunts. The traps can be individually electrically switched, are easily arrayable, and are amenable to batch fabrication. We have verified the predicted performance of the extruded traps by measuring holding of beads against flows and comparing to the model predictions. The results demonstrate that extruded quadrupolar traps exhibit strong particle confinement and that the modeling tools can be used for a priori design of dielectrophoresis-based single-particle traps.

© 2002 Elsevier Science B.V. All rights reserved.

Keywords: Dielectrophoretic levitation; Quadrupolar traps; Cell analysis

1. Introduction

Dielectrophoretic (DEP) traps use the interaction of an induced multipole with a non-uniform electric field to create a stable potential energy well in an electroquasistatic field [1]. Such traps have been used for a variety of applications, including micron and sub-micron particle capture [2–4], electrorotation [5], combination electrooptical tweezers [6], and UV-induced particle processing [7].

*Corresponding author. Tel.: +617-253-2094; fax: +617-258-5846.

E-mail address: voldman@mit.edu (J. Voldman).

Many different electrode configurations can be used to trap particles, but the two most common are the planar quadrupole trap [8] and the octopole field cage [9].

Current cellular analysis with DEP-based particle traps is mostly limited to investigating changes in the electrical properties of cells after stimulation—e.g., using electrorotation [10]. However, a large number of cell-based assays use luminescent probes—e.g., green-fluorescent protein [11], Ca^{2+} -sensitive fluorophores [12], and luciferase [13]. These probes can exhibit high specificity and permit investigation of a wide range of cellular pathways. Cell-based luminescent assays in DEP particle traps benefit from allowing one to expose cells to stimuli after they have been trapped. Such assays allow one to probe the dynamic response of cells (e.g., calcium kinetics) or continuously monitor individual cell responses during the addition of several reagents, each with its own time course. Such assays require single-particle traps that exhibit holding of cells against flow, because liquid will be the predominant stimulus carrier. In addition, performing such assays with arrays of single-particle DEP-based traps would allow one to probe cellular pathways on statistically significant cell populations with single-cell resolution.

The planar quadrupole and octopole DEP traps display very different characteristics of trapping against liquid flow. Only the octopole field cage is strong enough to hold cells against practical flows [14]. However, the octopole field cage suffers from fabrication challenges—e.g., electrode definition on thin ($<200\ \mu\text{m}$) substrates—and difficult packaging requirements—e.g., alignment of two opposed quadrupoles. In addition, the chamber height and quadrupole electrode separation cannot be independently altered, and the octopole field cage cannot be easily arrayed without the use of multilevel metallization. Thus, while the octopole field cage is more than adequate for single-particle investigations, it will be too cumbersome for use in arrays.

We have been interested in the development of DEP-based traps for large-scale single-particle holding to enable parallel single-cell luminescent assays. Thus, we require a DEP-based trap that can be easily arrayed, is amenable batch fabrication, exhibits strong holding against flow, and can be individually turned on and off to effect sorting. In order to design such a trap, we have taken advantage of the modeling tools that we have developed and used for the quantitative prediction of planar quadrupole trap performance [15]. We have used these tools to design a trap geometry that meets the requirements of our application, the result being the extruded quadrupole trap described below. We have also optimized the trap design with respect to three key system parameters. First, we specified the flow against which the trap must hold by limiting the time needed to introduce reagents into the system. Next, we limited the maximum electric field to which trapped cells could be exposed to minimize transmembrane loading. Finally, we minimized the fluid shear imposed on the cell to reduce the likelihood of shear-induced cellular responses.

The resulting device has been predicted and experimentally shown to hold beads against fluid flow with $>100\ \text{pN}$ of force, and is predicted to hold HL-60 cells with $\sim 40\ \text{pN}$ of force while keeping the induced transmembrane potential to $\sim 30\ \text{mV}$ and the fluid shear on the cells to $0.03\ \text{Pa}$. In addition we have manufactured arrays of these traps using a single metallization layer and incorporating single-trap control.

The fabricated traps are compatible with high-resolution fluorescence microscopy and operation with viable cells in high-conductivity (~ 1 S/m) buffers [16]. Thus, the trap design presented herein represents a viable alternative to the other field cages with advantageous characteristics for a variety of applications.

2. Materials and methods

2.1. Modeling

Modeling was performed using our previously described simulation tools [15]. Briefly, the model takes as inputs the electric-field data and other experimental parameters and computes the total force on the particle (cell or bead) everywhere in space. From this, the model determines if the total force on the particle in the trap stably goes to zero anywhere. Such points are called holding points, and represent where the particle will be held. By varying the applied flowrate for a given experimental condition, the modeling environment can determine when the holding points cease to exist and therefore the strength of the DEP particle trap.

Simulations encompassed both as-designed (no taper, and with as-drawn trap geometries) and as-fabricated trap geometries (described below). Drag forces were computed using a parabolic flow profile. Unless noted otherwise, the simulations were performed on polystyrene beads at a frequency of 20 MHz with a bead density, relative permittivity, and conductivity of 1.062 g/cm³, 2.5, and 10^{-4} S/m, respectively, in physiological saline (conductivity of 1 S/m, relative permittivity of 80), and simulating the dipole and quadrupole force orders. The chamber geometry for the relative design was 5 mm wide and 150 μ m high, and for the finalized design was 2 mm wide and 150 μ m high. Parameters for the HL-60 cell simulations were obtained from [17] and a cell radius of 6.25 μ m, membrane capacitance and conductance of 1.6 μ F/cm² and 0.22 S/cm², respectively, membrane thickness of 1 nm, and cytoplasmic relative permittivity and conductivity of 75 and 0.75 S/m, respectively, were used.

2.2. Electrode fabrication, packaging, and test setup

The process flow, packaging scheme, and test setup have been described elsewhere [18]. Briefly, 170 nm of Ti and 500 nm of Au were evaporated onto Pyrex wafers. The gold was pattern-etched with a potassium iodide-based etchant (Gold Etchant Type-TFA, Transene, Danvers, MA). The posts were made by electroplating gold (Orotemp 24, Technic Inc., Anaheim, CA) onto a 60- μ m thick SU-8 mold (SU-8 50, Microchem Corp., Newton, MA). Following electroplating, the SU-8 mold was stripped using a three-step process involving a DMSO-based photoresist stripper (Ashland Chemical, Pueblo, CO), an O₂ plasma ash, and a Nanostrip clean (Cyantek, Fremont, CA). The Ti layer was then stripped using a dilute HF:H₂O solution, followed by a second SU-8 photolithography step to define the chamber. The wafer was then die-sawed, fluid inlet and outlet holes were drilled

using a 0.75-mm diamond drill bit (C.R. Laurence, Los Angeles, CA), and a coverslip was glued to the SU-8 channel to complete the fluid chamber.

The chips were packaged by affixing them via double-sided tape to a ceramic carrier in which fluid inlet/outlet holes had been drilled. Wire bonds from the chip to the ceramic carrier provided electrical connections. The ceramic carrier interfaced with a ZIF-socket into which an aluminum block was inserted to provide o-ring-coupled fluid access to the chip. The ZIF-socket was also electrically connected to a circuit board that contained the drive electronics.

The chips were observed with an upright fluorescence microscope (Zeiss Universal, Carl Zeiss Inc., Thornwood, NY) and a video camera (TM-7CN, Pulnix America, Inc., Sunnyvale, CA). The packaged chip was of low profile so that it could be directly interfaced with high numerical aperture (and thus short-working distance) objectives, and the use of a standard coverslip as the channel ceiling allowed use with high-resolution microscope objectives. Flow was provided by a syringe pump (KD-101, KD Scientific, Boston, MA) using a 5 ml Hamilton luer-lock syringe (1005TLL, Reno, Nevada). The fluid path was provided by HPLC connectors and tubing (Upchurch Scientific, Oak Harbor, WA).

2.3. Beads and solutions

A stock solution ($\sigma_m = 0.01$ S/m) was made by taking DI water supplemented with 0.05% Triton X-100 (Sigma, St. Louis, MO) and further supplemented with appropriate amounts of Hank's Balanced Salt Solution (HBSS, GibcoBRL, Grand Island, NY), also with 0.05% Triton X-100, until the nominal conductivity was reached, as indicated by a Orion Model 125 conductivity meter (Beverly, MA). Solutions were filtered through a 0.45- μm filter (Micron Separations, Inc., Westborough, MA) and their conductivity was measured before each use. Polystyrene beads (incorporating 2% divinyl benzene), with density 1.062 g/cm³, in three diameters—7.58 μm (0.08 μm std. dev.), 10.00 μm (0.09 μm std. dev.), and 13.20 μm (0.89 μm std. dev.)—packaged as 10% solids in water were purchased from Bangs Laboratories (Fishers, IN). Fifteen microliters of each bead solution was washed twice in 1.5 ml of the stock solution and finally resuspended in 1.5 ml of stock solution. All bead solutions were refrigerated and used within 2 months.

2.4. Experimental protocol

Once beads were captured in the quadrupole trap, flow was initiated. In the parallel-plate flow chamber, beads experienced a transverse hydrodynamic force that tended to dislodge them from equilibrium at the center of the trap and thus acted as a destabilizing force. If the bead was held in the trap after 60 s, the bead was considered captured. Initial tests showed that the vast majority of beads held for 60 s were indefinitely held. The flowrate was adjusted to find the minimum flowrate (within 1 $\mu\text{l}/\text{min}$) at which the bead was released within 1 min. This is termed the “release flowrate”. Data were obtained from three different traps over a period of 2 weeks.

3. Design

We undertook the trap design by first settling on the basic electrode configuration—the quadrupole—and then optimizing the geometry of the quadrupole to improve its performance. These simulations were performed on beads because the *relative* comparison between different trap geometries will hold regardless of the specific particle. To finalize the electrode design and chamber geometry, we performed simulations on cells to converge to an *absolute* design that would meet the quantitative system parameters.

3.1. The extruded quadrupole

We decided to use a quadrupolar electrode arrangement for our basic trap geometry (Fig. 1A) because it gives two-dimensional confinement with a small number (i.e., four) of electrodes. The third dimension of confinement can be obtained from quadrupolar levitation interacting with the weight of the particle. We also decided against shaping the electrodes (beyond giving them circular cross-sections) because near the field minimum (where the particle can be expected to be held) any higher-order non-uniformities due to electrode shaping will be damped out, causing the field to appear quadrupolar.

With these choices in mind, we wanted to design a trap that was significantly stronger than the planar quadrupole trap, where strength is defined as the ability to hold particles against flow. Previous analysis of the planar quadrupole trap demonstrated that its weakness was due to the increase in particle height with voltage coupling with (1) decreasing electric field intensity with height (due to the planar structure of the electrodes) and (2) increasing exposure to drag forces with height [15].

We decided to overcome these disadvantages by using an extruded quadrupolar geometry, as shown in Fig. 1B. An extruded three-dimensional trap solves both of these problems and is amenable to batch fabrication. First, extending the electrodes

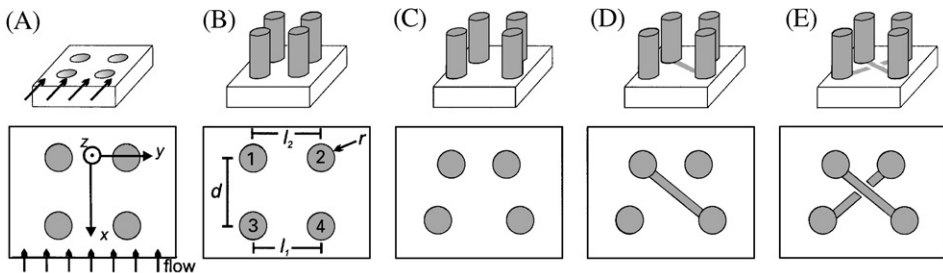


Fig. 1. Evolution of the extruded trap. (A) Four planar electrodes arranged in a square, along with the reference axes and the direction of flow. (B) Four cylindrical electrodes arranged in a square. Also shown are the geometric variables used in the trap optimization simulations and numerical labels for individual electrodes. (C) Four cylindrical electrodes arranged trapezoidally. (D) Introduction of wiring between two electrodes. (E) Final electrode configuration, showing the two shunts that restore the symmetry to the trap. For all these configurations, fluid flow and axes are as in (A).

in the z -direction can eliminate the field decay away from the substrate by adding axial symmetry. Second, the axial symmetry reduces the z -directed DEP forces and thus limits any increase in particle height with voltage. The top and bottom of the electrodes will break this symmetry and introduce z -directed DEP forces, but it certainly will be possible to limit the excursions in the z -direction and thus increase the holding.

We needed the height of the quadrupole electrodes to be greater than the characteristic cell diameter ($\sim 20 \mu\text{m}$), so that the electrodes would indeed appear to be posts to the cell and the capture cross-section would not be negligible. To meet these constraints, we chose a nominal electrode height of $50 \mu\text{m}$.

3.2. Electrode arrangement

The first parameter that we investigated was the electrode arrangement. We wanted to make it easy to load particles into the trap without compromising the trap strength. Entry into the trap is dominated by the potential energy barrier created by electrodes 3 and 4, while electrodes 1 and 2 largely determine the exit barrier and thus the trap strength. Thus, by increasing the separation of electrodes 3 and 4 with respect to the separation between 1 and 2, the trap should be easier to load and

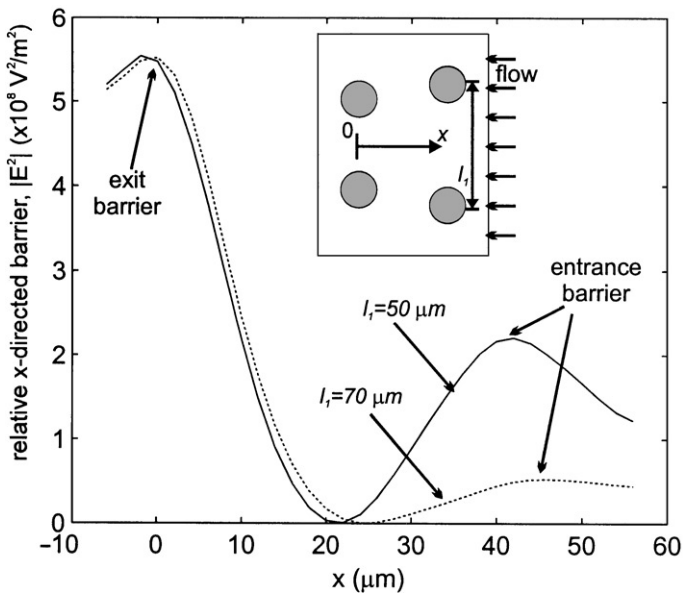
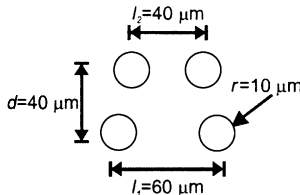


Fig. 2. Comparison of x -directed barriers for two trap geometries. The first geometry (—) is only slightly asymmetrical, with an entrance–electrode separation (l_1) of $50 \mu\text{m}$ and an exit–electrode separation (l_2) of $40 \mu\text{m}$. The second geometry (---) has the same exit–electrode separation but a $70 \mu\text{m}$ entrance–electrode geometry. Plotted is the $|\mathbf{E}|^2$ factor along the y -axis at a height of $16 \mu\text{m}$. The axes are as defined in the inset.

Table 1

Matrix for trap optimization. Shown is a top-down view of the initial trap geometry. Also shown are the variables that were varied, one at a time, to trace out the design space. Italic numbers indicate the starting trap geometry on which the variations were made

Initial geometry	Variable	Range of variation
	<i>R</i>	5, 10, 15 μm
	<i>L</i> ₁	50, 60, 70 μm
	<i>L</i> ₂	30, 40, 50 μm
	<i>D</i>	30, 40, 50 μm

still remain strong. Fig. 2 shows a plot of the $|\mathbf{E}|^2$ term (proportional to the DEP potential energy) along the x -axis for two differently asymmetric trap geometries under the same experimental conditions. The change in the entrance–electrode spacing from 50 to 70 μm barely affects the exit barrier height (at $x = 0$) but lowers the entrance barrier height $\sim 5 \times$, making the trap much easier to load.

To optimize the remaining aspects of the trap geometry we performed a series of simulations within a matrix of variations (Table 1), varying each parameter while holding the others constant. We varied the electrode radius, entrance and exit electrode separation, as well as the distance between the entrance and exit electrode pairs. Fig. 3 shows the results of varying these four electrode parameters. Here we plot the release flowrate at the same voltage for various designs. Given the monotonic nature of the release characteristics (described below), this gives an adequate comparison between designs. Also plotted is the maximum electric field in the vicinity of the particle, which is proportional to the induced transmembrane potential. We want to minimize this parameter while maximizing the release flowrate. The results show that changes in the post radius r and the exit–electrode separation l_2 dramatically affect both the holding and the electric field in fairly linear manners, while the other two parameters do not affect the holding. This is reasonable given that the inner distance between the posts is $l_2 - 2r$ and that this is the primary variable that will affect both the imposed electric field (at a given voltage) near the exit electrodes and the trap strength.

Fig. 3 also shows that increasing the strength of the trap by arranging the electrodes is accompanied by corresponding increases in the imposed electric field, and thus no improvement in trapping efficiency—holding relative to imposed electric field—is achieved. Because of this we chose the design in the middle of the design space (with dimensions shown in the figure of Table 1). Thus, we see that the model can be used to discriminate between parameters that result in a net gain in performance and those that do not.

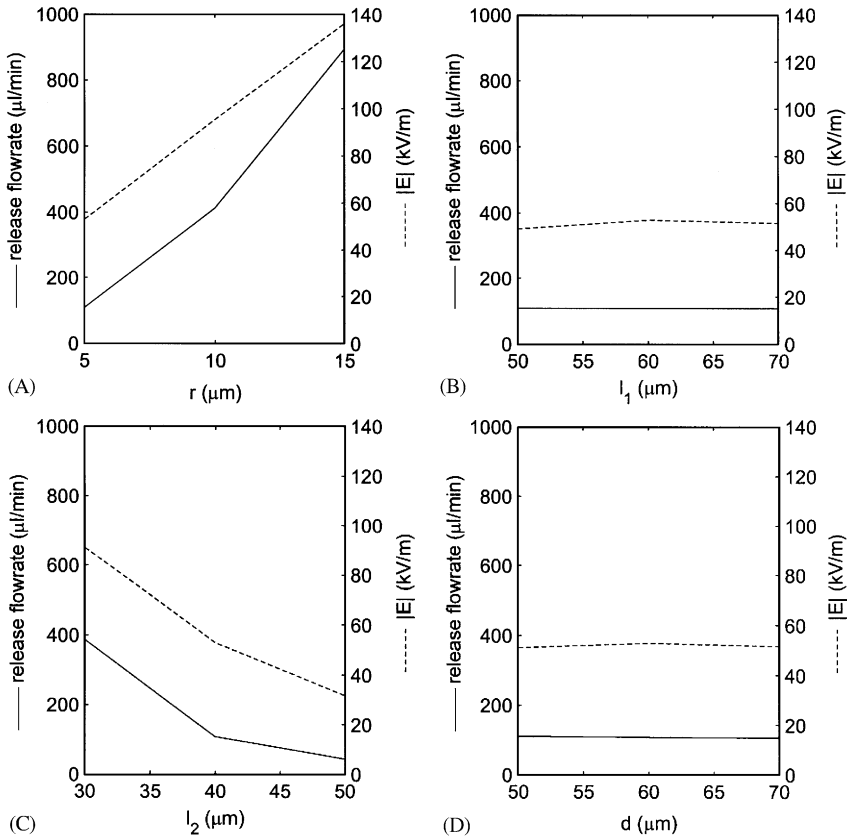


Fig. 3. Results of trap optimization simulations. Plotted are the release flowrate (—, left y -axis) electric field experienced by the particle at release (---, right y -axis) for various trap geometries defined in Table 1 under identical experimental conditions. Shown are variations in (A) electrode radius r , (B) entrance-electrode spacing l_1 , (C) exit-electrode spacing l_2 , and (D) trap length d .

3.3. Electrode switching

To individually control traps, we wanted to determine if only one electrode needed to be switched to “turn off” a whole trap. This would minimize the control circuitry and external chip connections. One way to accomplish this is to switch the polarity of one electrode in the quadrupole, thus eliminating the symmetric arrangement of potentials. The result of this is shown in Fig. 4. Here we plot the vector force fields in the xy -plane at the height of $16\ \mu\text{m}$ when the quadrupole is stimulated with alternating polarities (Fig. 4A), and when the polarity of electrode 2 is reversed (Fig. 4B). The change in polarity of one electrode is enough to disrupt the particle confinement and eject the particle. Thus, in the final trap design this electrode is wired to be switchable in this way. Although

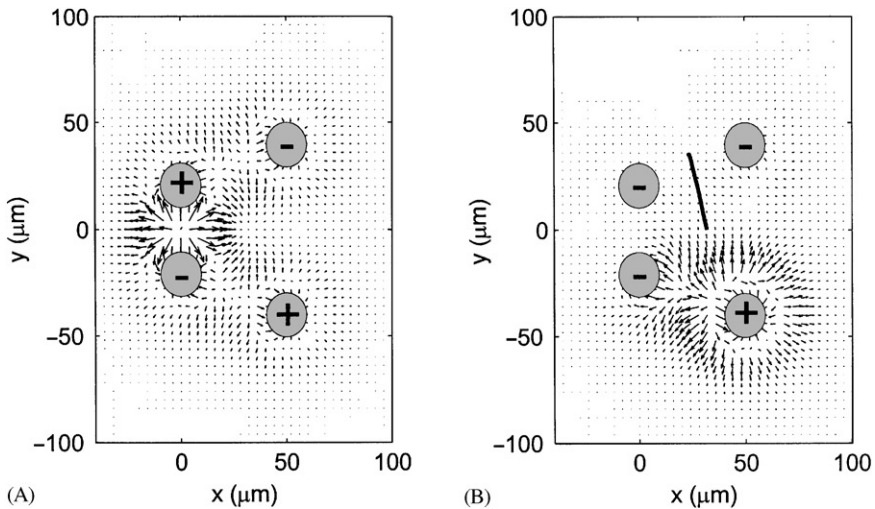


Fig. 4. Trap switching via one electrode. (A) A vector plot of the DEP force in the xy -plane at a height of $16\ \mu\text{m}$ when the trap is excited conventionally. (B) Plot of the same situation when the polarity of the top-left electrode is changed from $+V$ to $-V$. The black line shows the trajectory of a particle at the trapping point in (A) upon initiation of the excitation pattern in (B). The particle is ejected from the trap. This particular trap had $100\text{-}\mu\text{m}$ -tall posts with $d = 50\ \mu\text{m}$, $l_1 = 40\ \mu\text{m}$, and $l_2 = 80\ \mu\text{m}$.

the imposition of flow and the addition of substrate interconnects (described below) would change the trajectory of the ejected particle, the particle will still be ejected, which is the goal.

3.4. Substrate interconnects

For ease of fabrication, we chose to limit metalization to one layer and no dielectric layers. Although the following discussion of how to compensate for this becomes irrelevant if multilayer metalizations and/or insulators can be used, it nonetheless displays the use of the modeling environment to compensate for practical constraints.

The optimal way to wire an array of traps within a small area and keep the lead count low is to tie one pair of electrodes to the same potential by connecting them through the middle of the trap, as shown in Fig. 1D. Simulating the holding characteristic of this trap, we show in Fig. 5 that this trap is much weaker than the trap with no wiring (Fig. 1C). The reason that the interconnected trap is much weaker than the “ideal” trap is that the interconnect disrupts the symmetry of the trap, displacing the particle from the symmetrical minimum and thus reducing the trap strength.

One approach towards restoring the strength of the trap given the need for the interconnect would be to restore its symmetry. We empirically designed and simulated a number of possible wiring schemes to try to restore the trap strength.

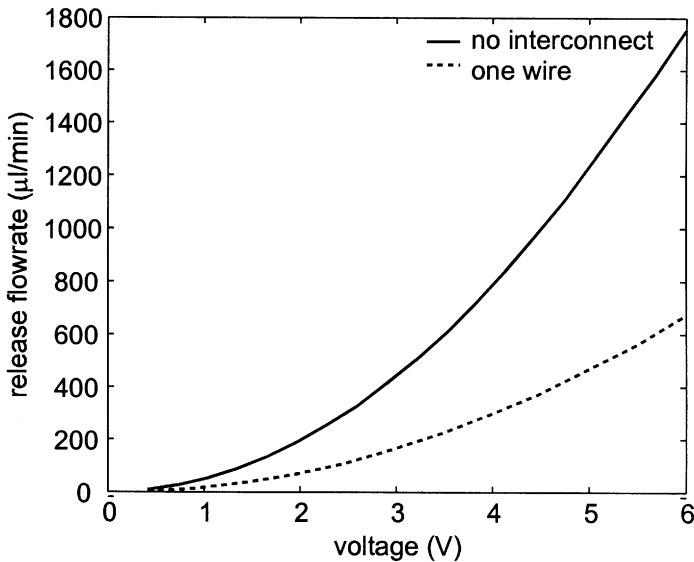


Fig. 5. Holding characteristic of the single-wire trap. Plotted is the release flowrate versus voltage for the trapezoidal trap with (---) and without (—) a substrate interconnect between electrodes 1 and 4. The introduction of the substrate interconnect drastically reduces the holding in the trap and thus its performance.

The designs and simulated release flowrates at a given voltage are shown in Fig. 6. Although several wiring schemes (#4–#6) perform equally well in restoring the trap strength, wiring scheme #4 delivers the most restoration of the holding while minimizing the encountered electric field. We have thus chosen wiring scheme #4 for these traps, shown in Fig. 1E.

The imposition of the substrate interconnects alters the trap geometry such that the assumption of axial symmetry no longer holds. For the final trap (Fig. 1E), then, the question arises as to whether it will suffer from the shortcomings of the planar quadrupole—i.e., an increase in particle height versus voltage and a decrease in the electric field away from the substrate. For this trap, simulations show that the particle levitation height is insensitive to voltage because the upward DEP force from the substrate interconnects is balanced by the downward DEP force due to the top of the electrodes (data not shown). Thus, the particle attains a constant height (versus voltage), which leads to strong holding. Given the constant particle height, the latter concern is unfounded because the cylindrical electrodes maintain the electric field at that height.

Fig. 5 also shows the monotonic nature of the holding characteristic for the extruded traps, irregardless of specific geometry, and thus validates our earlier assumption that comparing different geometries at only one voltage gives an adequate comparison (Figs. 3 and 6).

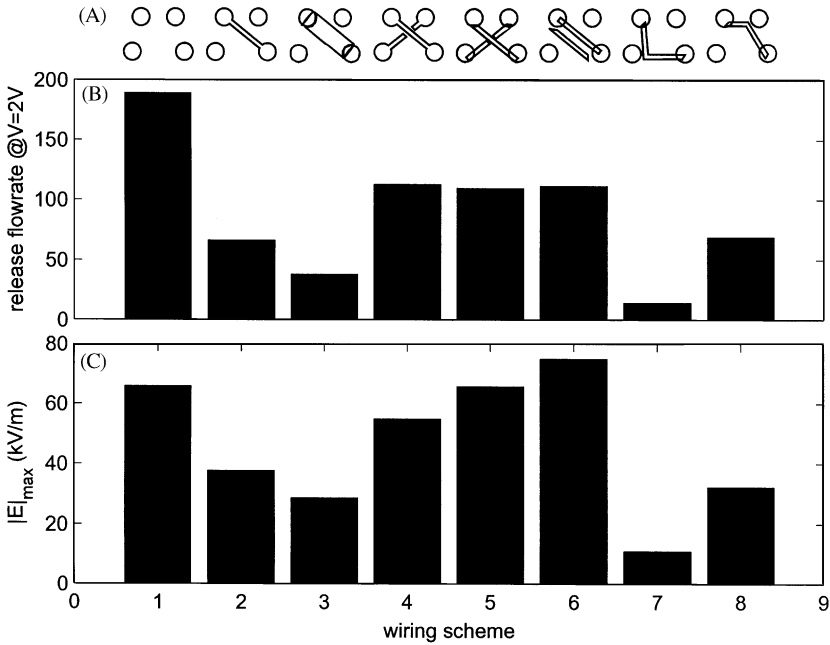


Fig. 6. Results from various wiring schemes. (A) Shown are various empirically designed wiring schemes. The two left-most schemes are, from left to right, with no internal wiring and a single interconnect. The rest of the schemes are designed to restore the performance of the trap. (B) The release flowrate at 2 V due to the wiring schemes in (A). The left-most result, from a trap with no interconnect, possesses the highest release flowrate and is the ideal trap. (C) The electric field encountered in the various traps in (A) at 2 V.

3.5. System-level design

Given an adequate relative design, we can now undertake a system-level design to determine the actual chamber geometry and operating regimes that will meet the quantitative system parameters. For a given application, different constraints will need to be met. We show an analysis for our application—holding of HL-60 cells against flows for parallel assays. The goal of this analysis is to determine a chamber height and width that will allow operation within the system parameters. For this specific design, we have chosen to fix the chamber width at 2 mm and only explore variations in chamber height. Below we describe the three quantitative system parameters and their dependencies on the chamber height.

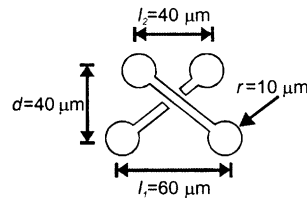
The primary quantitative requirements are described in Table 2. The first requirement is that the time needed to introduce reagents into the chamber be less than 2 min, in order to operate the trap arrays in a judicious manner. Given a certain chamber geometry and tubing void volume (V_0), the minimum release flowrate (Q_{rf}) needed to introduce reagents to the chamber in that time will be

$$Q_{rf} = (wlh + V_0)/t_f, \tag{1}$$

Table 2

Final system-level design parameters. Shown are the target and final values for the five system parameters in the design. Below that the trap dimensions and operating characteristics necessary to obtain those values are displayed

Parameter	Target value	Final value
Time to load chamber (s)	120	120
Shear on cells (Pa)	<0.1	0.03
Transmembrane load (mV)	<70	~30
Electrical switchability	Y	Y
Arrayability	Y	Y
Operating voltage (V)		3 V
Operating frequency (f)		20 MHz
Release flowrate		12 $\mu\text{l}/\text{min}$
Chamber height (h)		150 μm
Chamber width (w)		2 mm
Trap dimensions		



electrode height = 50 μm

where w , l , and h are the chamber width, length, and height, respectively, and t_f is the fill time. Because the void volume will likely be much larger than the chamber volume (for our analysis, 20 μl), the needed flowrate will only be weakly dependent on the chamber geometry.

The second system parameter is that the maximum shear on the cells be less than 0.1 Pa (1 dyn/cm²) to minimize shear-induced physiological effects. Arterial shear stress is about 1.5–2.0 Pa (15–20 dyn/cm²) [19], and so we want to keep shear stress levels well below that value, or about 0.1 Pa (1 dyn/cm²). Near the chamber wall, where the cell will be, the cell will feel approximately the wall shear resulting from plane Poiseuille flow, which is [20]

$$\tau_{\text{ss}} = 4U_c\eta/h = \frac{4}{h} \left(\frac{3Q_{\text{rf}}}{2A} \right) \eta = \frac{6Q_{\text{rf}}}{wh^2} \eta, \quad (2)$$

where τ_{ss} is the shear stress, U_c is the centerline flow velocity, A is the cross-sectional area and η is the viscosity of the water. In this case the shear is strongly dependent on the chamber height ($1/h^2$) if the required release flowrate (Q_{rf}) is only weakly dependent on the chamber height.

The final system parameter is that the maximum externally imposed transmembrane potential on the cells be less than the endogenous transmembrane potential

(~ 70 mV). We modeled the HL-60 cells as membrane-covered spheres using physical and electrical properties from [17]. In this case, the imposed transmembrane potential when the cells are placed in a uniform electric field is [21]

$$|V_{\text{tm}}| = \frac{1.5|\mathbf{E}|R}{\sqrt{1 + (\omega\tau)^2}} \quad (3)$$

where $|\mathbf{E}|$ is the applied electric field, R is the cell radius, ω is the radian frequency of the applied field and τ is the time constant given by

$$\tau = \frac{RC_m(\rho_{\text{cyto}} + 1/2\rho_{\text{med}})}{1 + RG_m(\rho_{\text{cyto}} + 1/2\rho_{\text{med}})}, \quad (4)$$

where C_m and G_m are the membrane capacitance and conductance, respectively, and ρ_{cyto} and ρ_{med} are the cytoplasmic and medium resistivities, respectively. This model does not take into account the high-frequency saturation of the voltage [21]. Minimizing the imposed potential requires operating at the highest possible frequency, which in our case is 20 MHz, constrained by the experimental apparatus. At this frequency the imposed load on the HL-60 cells is $\sim 20 \times$ smaller than at DC. Thus, we can set a limit on the maximum electric field to which the cells can be exposed, by manipulating Eq. (3), to $\sim 1.8 \times 10^5$ V/m.

To determine how the imposed transmembrane potential will scale with the chamber height, we can use the fact that the transmembrane potential is proportional to the imposed electric field (Eq. (3)) and thus proportional to the applied voltage. Then, given the approximately quadratic nature of the holding characteristic with applied voltage (Fig. 5) and the linearity of the volume flowrate with chamber height, we can introduce chamber height as a parameter. For any given holding characteristic (e.g., Fig. 5), we can account for variations in chamber height by

$$Q_{\text{rf}} = \alpha V^2 \frac{h}{h_0}, \quad (5)$$

where α is some fitting parameter, V is the applied voltage, h is the varying chamber height, and h_0 is the nominal chamber height at which the holding characteristic was simulated. Thus, if a given Q_{rf} is needed to meet the system parameters then the voltage needed to hold against that flow will scale as

$$V = \sqrt{\frac{Q_{\text{rf}}h_0}{\alpha h}}, \quad (6)$$

which goes as $1/\sqrt{h}$. Thus, increasing the chamber height should decrease the voltage needed, and thus the electric field experienced by the cells.

Given these dependencies, we next performed iterative simulations varying the chamber height to converge to a final design. First, we performed simulations on a given set of chamber dimensions to determine the holding characteristics of HL-60 cells. Then, we scaled those results to other chamber heights by ratioing the results (as in Eq. (5)). Next, using the chamber height as a parameter, we calculated the flowrate needed for 2-min chamber loading from Eq. (1), the voltage that is therefore

required (from the scaled holding characteristic), and thus the transmembrane potential experienced by the cell. The result of this analysis is shown in Fig. 7. The figure confirms the behaviors predicted above: the flowrate needed (Fig. 7A) is fairly insensitive to the chamber height (and thus volume), while the operating voltage, induced transmembrane potential, and shear on the cells decrease with increasing chamber height. In all cases the transmembrane potential is < 70 mV and the shear on the cells is less than 0.1 Pa. Thus, there is an operating point that will meet the specifications of Table 2. We chose a chamber height of $150\ \mu\text{m}$ to satisfy these requirements, giving an operating voltage of ~ 3 V and a release flowrate of $\sim 12\ \mu\text{l}/\text{min}$. This release flowrate corresponds to a holding force of ~ 50 pN.

The final designed trap geometry is shown in Fig. 1E. The extracted system-level parameters for using the final design with cells are shown in Table 2. As shown, the

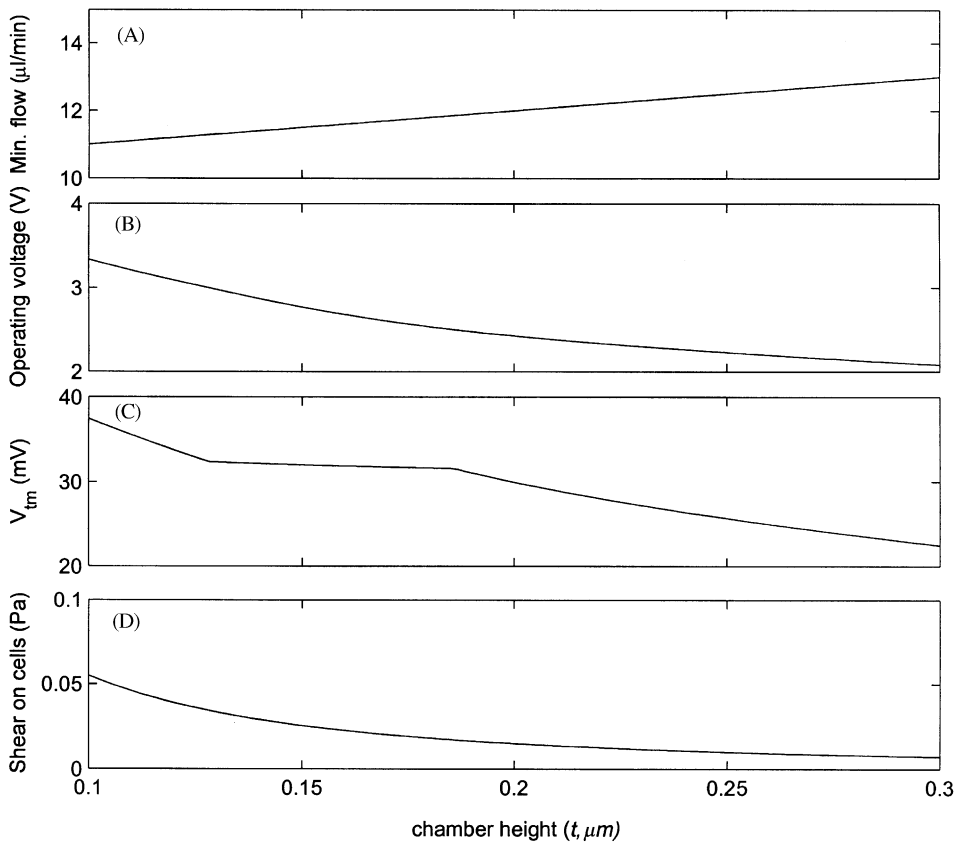


Fig. 7. System-level design of chamber height for use with HL-60 cells. (A) Plotted is the minimum flowrate needed to fill the chamber in 120 s (from Eq. (1)) as the chamber height, and thus chamber volume, varies, for a void volume of $20\ \mu\text{l}$. (B) The voltage, obtained from the holding characteristic (not shown), needed to sustain the flowrate in (A). (C) The transmembrane potential encountered by the cell at the voltage in (B). (D) The shear on the cells at the operating flowrate in (A), from Eq. (2).

trap and chamber geometries meet all the system parameters. Thus, using our modeling tools and the underlying physics of the situation we were able to determine absolute trap and chamber geometries that meet the requirements of the proposed application.

4. Analysis

In order to ensure that the design process was accurate, we performed release flowrate experiments on our fabricated traps to demonstrate that we had indeed predicted the strength of the traps. We used beads instead of cells for these experiments because their more uniform and well-known properties make for a more accurate comparison. Operation with cells will be described elsewhere [16].

4.1. Arrayability

Fig. 8 shows SEMs of the completed traps, illustrating the fact that they are easily arrayable, even with one level of metal. We fabricated several configurations of trap arrays— 1×4 , 1×8 , and 2×4 . Even though we did not optimize the trap spacing, we were able to space them $100 \mu\text{m}$ apart, allowing for a fairly high linear trap density—10 traps/mm.

4.2. Trap switching

We first verified several qualitative aspects of device operation. We loaded the traps with $10.0\text{-}\mu\text{m}$ polystyrene beads and individually toggled the switchable electrodes. Fig. 9 shows three sequential movie frames illustrating that we can turn traps off independent of each other. Under flow, the released bead flows away when only one electrode is toggled between $+V$ and ground.

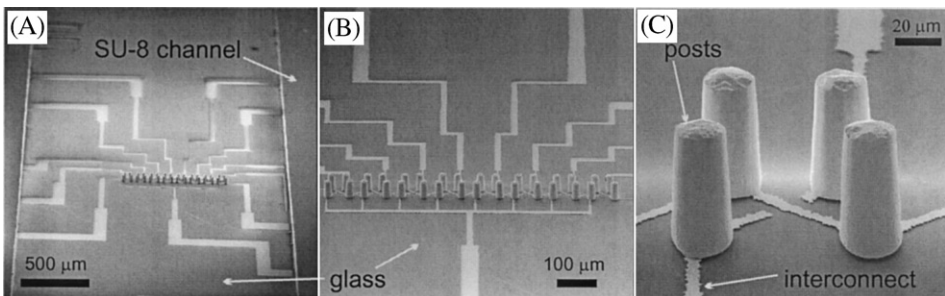


Fig. 8. Final SEMs of the completed devices. (A) A 1×8 array in an SU-8 channel. (B) A close-up of the array. (C) A close-up of a single trap.

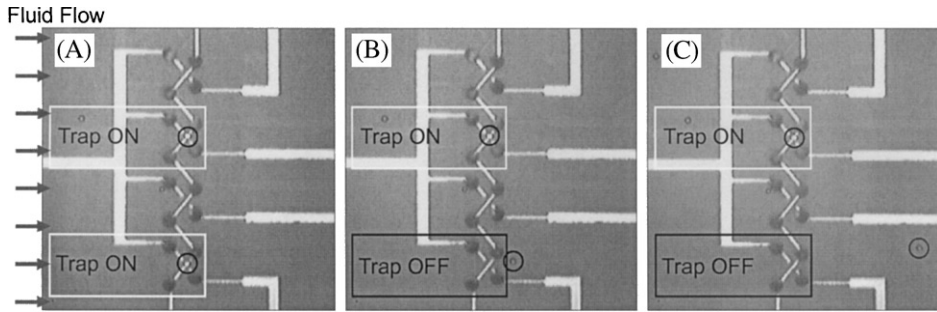


Fig. 9. Movie frames showing electrical control of the traps. (A) Flow ($3 \mu\text{l}/\text{min}$) was applied from left to right, with two $10.0\text{-}\mu\text{m}$ beads held in each of two traps. (B and C) The bottom trap was turned off by switching its bottom-right electrode, causing the bead in the top trap to flow away while the bead in the top trap was held. Traps were energized at 1.5V and 1MHz .

4.3. Holding characteristics with beads

In order to be able to compare the predictions to experimental analysis, we performed measurements on the actual as-fabricated devices to extract the as-fabricated geometry. We then used these as-fabricated parameters to predict the performance of the traps. Although most as-fabricated geometrical parameters were close to the design values, one significant deviation was that the electrodes tapered along their length (see Fig. 8C). This removed the strict axial symmetry of the electrodes, introducing an upward-directed DEP force. Thus, we attempted to characterize this taper, and our measurements indicated that the posts had top diameters of $18\text{--}20 \mu\text{m}$ with a $2\text{--}3^\circ$ taper.

We performed experiments to obtain the holding characteristics of these traps. We loaded the traps with single beads of various sizes and then determined the minimum flowrate needed to dislodge the beads—the release flowrate. The results are shown in Fig. 10. The error bars represent experimental errors of 1 std. dev. All release flowrate measurements were taken 3–8 times and on average 4.3 times. The data demonstrate that the holding in these traps is size selective with larger beads exhibiting stronger holding, as one would predict given the R^3 dependence of the dipolar DEP force.

In Fig. 10A–C we also show comparisons between the experimental results and the modeling using electrodes with a $3.5\text{-}\mu\text{m}$ difference in the top and bottom cross-sectional diameters (corresponding to a 2° taper). For these simulations we used the measured as-fabricated chamber height of $159.5 \mu\text{m}$ as well as the properties of the actual experimental situation (in this case, solution conductivity of 0.01 S/m , bead conductivity of $2 \times 10^{-4}\text{ S/m}$, and applied frequency of 1 MHz). The smaller model prediction in each subplot corresponds to a post diameter of $18\text{--}21.5 \mu\text{m}$ (top cross-sectional diameter and bottom cross-sectional diameter), while the larger model prediction corresponds to a post diameter of $19\text{--}22.5 \mu\text{m}$. As stated

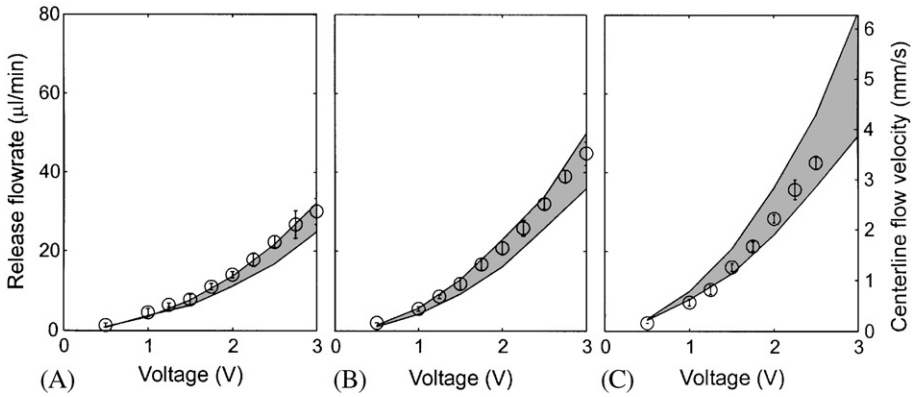


Fig. 10. Model predictions of the holding characteristics. The data is shown as discrete points (o) while the simulation results are shown as a gray patch whose lower bound corresponds to the 18–21.5-µm diameter posts and upper bound to the 19–22.5-µm posts. The data and predictions are shown for (A) 7.6-µm, (B) 10.0-µm, and (C) 13.2-µm bead diameters. The predictions were calculated using the parameters described in Section 2 except that the as-fabricated chamber height was 159.5 µm and the experimental solution conductivity was 0.01 S/m, bead conductivity was 2×10^{-4} S/m, and applied frequency was 1 MHz.

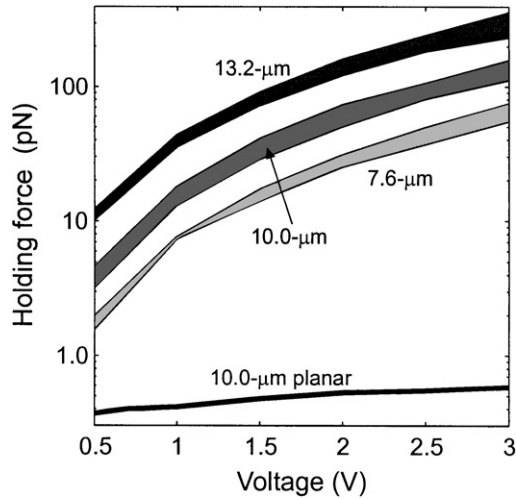


Fig. 11. Extracted holding forces of the extruded quadrupole traps. Plotted are holding forces for 13.2-µm (top patch, dark gray), 10.0-µm (middle patch, medium gray), and 7.6-µm (lower patch, light gray) beads using across the range of geometrical variations. The upper bound for each bead diameter corresponds to the 19–22.5-µm posts and the lower bound to the 18–21.5-µm posts. Parameters for the predictions are as for Fig. 10. Also shown (—) for comparison are the results for 10.0-µm beads in the planar quadrupole.

before, this is within the limit of the measurements of the electrode geometry. While the geometrical measurements span a wider space than the two simulation results shown here, we chose these two geometries within that space for these predictions. Including more of the geometrical measurement space in the predictions would only lead to a looser fit of the data and would not affect the conclusions.

The first feature to notice is that for all bead sizes the experimental data are bounded by the predictions. Thus, within the limit of our measurements of the trap geometry, we have absolutely predicted the performance of these traps. Second, because the traps are working as predicted we have also validated the design methodology.

With confidence in the model's results we can extract the holding forces from the simulations, as shown in Fig. 11. The results show the greatly increased strength of the new trap, as compared to the planar trap. For instance, a 10.0- μm bead is held with 65 pN of force at 2 V, as opposed to the 0.5 pN of the planar quadrupole. Thus, the extruded trap is $> 100 \times$ stronger than the planar trap.

5. Discussion

5.1. Model and trap validation

The results described above demonstrate the utility of our modeling environment for designing DEP-based traps for potential bioscience applications. We have been able to a priori design a trap geometry that could meet our system parameters without performing trial-and-error experiments. In addition, the geometry used for the extruded traps is much more complicated than most existing DEP-based traps, involving an asymmetric electrode placement, exposed wiring within the trap, and the tapered three-dimensional profile of the posts. Despite all of these challenges, the model has been successful in predicting the performance of these traps to the limit of our ability to make measurements; this is more than adequate for bioscience applications, as variations in a population of cells will be much larger than any variations encountered herein. The results also demonstrate an internal consistency to the design process—the modeling and the trap are both validated by these measurements. This validation, coupled with the results from the planar quadrupole, strongly suggests that such modeling could be useful in the future.

The fact that the data and modeling predictions agree strongly suggests that the 1-D Poiseuille flow profile used in the modeling adequately captures the behavior of particles in these traps. This is reasonable given that at the low Reynolds number flows utilized in these microsystems, spatial non-uniformities in the flow caused by the posts will persist on a characteristic length scale of order the post diameter, and thus will be minimal at the center of the trap. In addition, the agreement between modeling and experiment suggests that there we are not inducing any measurable electrothermal or other electrokinetic flows in our systems, at least at our operating conditions [22,23].

5.2. The extruded quadrupole

The extruded quadrupole trap designed herein possesses several advantageous characteristics for use as a single-particle trap. First, it exhibits extremely strong holding that is monotonic with voltage. The extracted holding forces easily reach 50–150 pN for reasonably sized beads. These forces are comparable to optical tweezers [24]. In addition, they are at least as strong as the octopole field cage [14]; analysis shows that the octopole field cage gives ~ 20 pN of holding for similar particles (data not shown).

Second, the trapezoidal electrode arrangement makes the extruded quadrupole trap easier to load than a symmetrical quadrupole or octopole trap. This is due to the relative lowering of the entrance barrier without affecting the trap strength, because of the asymmetry of the electrode placement.

Third, the extruded quadrupole has been shown to be amenable to batch fabrication, and can be arrayed, even with only one layer of metal. We have fabricated 1×4 , 1×8 , and 2×4 arrays of these traps, all with one metallization layer (Fig. 8). Another extruded quadrupole electrode configuration that was serially fabricated does not display these characteristics [7]. In addition, there are no reports of the quantitative design or operation of this trap.

Fourth, the extruded quadrupole does not have to be fabricated on fragile thin glass wafers for high-quality optical access, as the octopole field cage does, and does not have alignment steps during packaging. The tradeoff, of course, is that the process flow for fabricating these traps is significantly more complex than with the planar quadrupole trap or octopole field cage.

Finally, the extruded quadrupole decouples the chamber height from the characteristic trap dimension. Thus, we can independently vary chamber height and electrode spacing, allowing us to more easily meet system requirements. For instance, by making the electrode height $1/3$ of the chamber height, as we have done here, we protect the trapped particles from the strongest drag forces, allowing us to impose higher volume flowrates. This gives us a net decrease in the time needed to fill the chamber, the imposed electric field (because we can operate at lower voltages) and the shear on the cell (because of the strong dependence of the shear on the chamber height (Eq. (2)).

5.3. Outlook for future trap design

Given the knowledge obtained about trap design, we can give qualitative speculations as to how to make future traps even stronger. We should stress, however, that strength is not everything. Other system parameters, given that the strength is adequate, may become “bottlenecks”. Nevertheless, several things are apparent.

First, one reason for the high trap strength is that the low height of the particle above the substrate shields it from the drag force. An easy way to increase the strength even further is to lower that height. Analysis of the model results shows that the particles average about $\sim 16 \mu\text{m}$ above the surface and thus could be lowered

(data not shown). Several ways exist to accomplish this. First, the upward DEP force is due to both the slope of the posts and the wiring in the center of the trap. Removing the effect of the wiring by passivating it and tailoring the slope of the posts (perhaps even making them reentrant) could tailor the height of the particle, even pushing it against the substrate, thereby maximally shielding it from the flow.

The modeling also demonstrates that it is difficult to extract stronger holding without also increasing the imposed electric fields. At least within the design space investigated here, changes in electrode arrangement did not yield improvement in holding relative to imposed field (Fig. 3). However, the modeling was extremely useful for discerning which substrate interconnect scheme restored the most holding relative to the imposed field (Fig. 6). Thus, there is use in trying to optimize this variable, as it is crucial for use with cells.

From a fabrication/packageing standpoint, making robust traps is crucial. The current trap geometry is very stable during operation—not a single post has been damaged after packaging. However, gold is soft, and the posts can easily get bent during fabrication steps, especially wet steps. This can be alleviated by (1) using a different geometry without posts, (2) increasing the diameter of the posts, (3) encapsulating the posts during fabrication, or (4) using a harder metal.

Finally, the strong sensitivity of the predicted trap performance on the taper angle (Fig. 10) suggests that this specific trap geometry is not robust towards processing variations. Designing a trap where taper angle does not affect the position of the particle or the electric field strength, such as a trap that forces the particle to the substrate, should be much more stable in this regard.

6. Conclusions

We have undertaken the design of an improved DEP-based single-particle trap with characteristics that can meet the quantitative requirements of our application. Through extensive use of our previously developed modeling tools, we have designed an extruded quadrupole trap with an asymmetric trapezoidal geometry. It can be easily arrayed and is electrically switchable. The trap also incorporates substrate shunts to improve holding when only one layer of metal is used with no dielectric. Through the evaluation of the design in terms of system parameters, we have determined operating characteristics and chamber geometries that will result in successful operation. We have also described the results of initial tests with the extruded traps to demonstrate that they indeed operate as designed. The predicted holding characteristics, once adjusted for the actual geometries of the fabricated device, are very close to the observations. This demonstrates that our modeling environment can be used for predictive design of traps much different than those it was validated with, and that it thus is a truly useful tool. In addition, these results introduce the extruded quadrupole trap, which has many potential applications.

Acknowledgements

We would like to thank the Microsystems Technology Laboratory at MIT for fabrication help. This work was supported by Kodak and NSF graduate fellowships (JV) as well as the Alliance for Cellular Signaling (NIGMS #1U54GM62114-01).

References

- [1] T.B. Jones, *Electromechanics of Particles*, Cambridge University Press, Cambridge, 1995.
- [2] T.B. Jones, G.W. Bliss, Bubble dielectrophoresis, *J. Appl. Phys.* 48 (1977) 1412–1417.
- [3] T.B. Jones, J.P. Kraybill, Active feedback-controlled dielectrophoretic levitation, *J. Appl. Phys.* 60 (1986) 1247–1252.
- [4] N.G. Green, H. Morgan, J.J. Milner, Manipulation and trapping of sub-micron bioparticles using dielectrophoresis, *J. Biochem. Biophys. Methods* 35 (1997) 89–102.
- [5] C. Reichle, T. Muller, T. Schnelle, G. Fuhr, Electro-rotation in octopole micro cages, *J. Phys. D* 32 (1999) 2128–2135.
- [6] G.R. Fuhr, C. Reichle, Living cells in opto-electrical cages, *Trac – Trends Anal. Chem.* 19 (2000) 402–409.
- [7] G. Fuhr, C. Reichle, M. Stuke, Processing of micro-particles by UV laser irradiation in a field cage, *Appl. Phys.* 69 (1999) 611.
- [8] G. Fuhr, W.M. Arnold, R. Hagedorn, T. Muller, W. Benecke, B. Wagner, U. Zimmermann, Levitation, holding, and rotation of cells within traps made by high-frequency fields, *Biochim. Biophys. Acta* 1108 (1992) 215–223.
- [9] T. Schnelle, R. Hagedorn, G. Fuhr, S. Fiedler, T. Muller, 3-Dimensional electric-field traps for manipulation of cells—calculation and experimental verification, *Biochim. Biophys. Acta* 1157 (1993) 127–140.
- [10] C. Reichle, T. Schnelle, T. Muller, T. Leya, G. Fuhr, A new microsystem for automated electrorotation measurements using laser tweezers, *Biochim. Biophys. Acta—Bioenerg.* 1459 (2000) 218–229.
- [11] R.Y. Tsien, The green fluorescent protein, *Annu. Rev. Biochem.* 67 (1998) 509–544.
- [12] J.R. Sotelo, J.C. Benech, *Calcium and Cellular Metabolism: Transport and Regulation*, Plenum Press, New York, 1997.
- [13] G.A. Rutter, H.J. Kennedy, C.D. Wood, M.R.H. White, J.M. Tavare, Real-time imaging of gene expression in single living cells, *Chem. Biol.* 5 (1998) R285–R290.
- [14] T. Schnelle, T. Muller, G. Fuhr, Trapping in AC octode field cages, *J. Electrostatics* 50 (2000) 17–29.
- [15] J. Voldman, R.A. Braff, M. Toner, M.L. Gray, M.A. Schmidt, Holding forces of single-particle dielectrophoretic traps, *Biophys. J.* 80 (2001) 531–541.
- [16] J. Voldman, M. Toner, M.L. Gray, M.A. Schmidt, A microfabrication-based dynamic array cytometer, *Anal. Chem.* 74 (2002) 3984–3990.
- [17] Y. Huang, X.-B. Wang, F.F. Becker, P.R.C. Gascoyne, Introducing dielectrophoresis as a new force field for field-flow fractionation, *Biophys. J.* 73 (1997) 1118–1129.
- [18] J. Voldman, M. Toner, M.L. Gray, M.A. Schmidt, A dielectrophoresis-based array cytometer, *Transducers '01*, Munich, Germany, 2001.
- [19] H.-J. Hsieh, N.-Q. Li, J.A. Frangos, Shear stress-induced gene expression in human endothelial cells, in: E. Bell (Ed.), *Tissue Engineering: Current Perspectives*, Birkhauser, Boston, 1993, pp. 155–166.
- [20] W.M. Deen, *Analysis of Transport Phenomena*, Oxford University Press, New York, 1998.
- [21] H.P. Schwan, Dielectrophoresis and rotation of cells, in: E. Neumann, A.E. Sowers, C.A. Jordan (Eds.), *Electroporation and Electrofusion in Cell Biology*, Plenum Press, New York, 1989, pp. 3–21.

- [22] N.G. Green, A. Ramos, A. Gonzalez, A. Castellanos, H. Morgan, Electrothermally induced fluid flow on microelectrodes, *J. Electrostatics* 53 (2001) 71–87.
- [23] N.G. Green, A. Ramos, H. Morgan, AC electrokinetics: a survey of sub-micrometre particle dynamics, *J. Phys. D* 33 (2000) 632–641.
- [24] K. Svoboda, S.M. Block, Biological applications of optical forces, *Annu. Rev. Biophys. Biomol. Struct.* 23 (1994) 247–285.